applied sciences

MDPI

Article

Icing Wind Tunnel Test Campaign on a Nacelle Lip-Skin to Assess the Effect of a Superhydrophobic Coating on Ice Accretion

Filomena Piscitelli *, Salvatore Palazzo and Felice De Nicola

Italian Aerospace Research Centre, CIRA, Via Maiorise, 1, 81043 Capua, Italy; s.palazzo@cira.it (S.P.); f.denicola@cira.it (F.D.N.)

* Correspondence: f.piscitelli@cira.it

Abstract: The formation of ice on nacelle causes the reduction or loss of aerodynamic performance, fuel consumption increases, reduced thrust, and the ingestion of ice, which can damage the engine. The piccolo tube anti-icing employed as an active ice protection system has limitations in terms of performance losses and energy costs. Furthermore, according to the FAA regulation, it cannot be activated during takeoff and initial flight phases in order to avoid engine thrust reduction. This work reports on an icing wind tunnel test campaign performed at initial flight phases conditions on the M28 PZL nacelle before and after the application of a superhydrophobic coating in order to study the effect of wettability on ice accretion. Results highlighted that an ice thickness reduction of −49% has been recorded at −12 °C, matched to an increase in the impingement length of 0.5%. At 95 m/s and at 420 s of exposure time, the ice thickness was reduced by −27% and −14%, respectively, whereas the impingement length reductions were −9.6% and −7.6%. Finally, an ice thickness reduction of −8% was observed at a liquid water content of 1 g/m^3, matched to an increase in the impingement length of 3.7% and to a reduction in length and number of the frozen rivulets.

Keywords: superhydrophobic coatings (SHC); nacelle lip-skin; passive ice protection system; icing wind tunnel tests

Citation: Piscitelli, F.; Palazzo, S.; De Nicola, F. Icing Wind Tunnel Test Campaign on a Nacelle Lip-Skin to Assess the Effect of a Superhydrophobic Coating on Ice Accretion. *Appl. Sci.* **2023**, *13*, 5183. https://doi.org/10.3390/app13085183

Academic Editor: Theodore E. Matikas

Received: 23 March 2023
Revised: 15 April 2023
Accepted: 19 April 2023
Published: 21 April 2023

1. Introduction

Ice accretion on the nacelle lip-skin surface which occur upon flying through clouds containing super cooled water droplets (SWD) can result in a reduction or a loss of aerodynamic performance due to the formation of non-aerodynamic profile [1,2]. When this occurs, the fuel consumption increases due to the higher drag force, and the thrust reduces as a consequence of the restriction of airflow through the fan due to ice accumulated on the inner surface portion of the nacelle lip-skin [3]. The worst scenario occurs when broken ice particles are absorbed, the ingestion of which can critically damage the engine. For these reasons, protection against icing is required as it is a potential cause of aircraft crashes. A typical anti-icing system used for the nacelle is the piccolo tube anti-icing (PTAI), which is one of the most popular hot-bleed-air anti-icing devices utilized for wings, among others [4–6]. The parameters affecting the thermal performance of the PTAI include the hot air mass flow rate, jet spacing, the distance from the holes to the surface, the impingement angle, etc. [7]. This high-performance system is better than other ice protection systems with respect to efficiency and reliability; nevertheless, it has limitations in terms of performance losses, energy costs, complexity, weight, and hotspot issues [8].

Furthermore, the engine nacelle is mainly exposed to the icing environment with SWD during the takeoff and the initial climb phases of flight [1,9]. According to the Federal Aviation Administration regulation, the anti-icing systems cannot be activated until the aircraft reaches 400 feet above the takeoff surface to avoid engine thrust reduction [10]. Therefore, the PTAI cannot protect the nacelle against ice accretion during these two flight

phases. Therefore, it could be highly desirable, mainly in these two flight phases, to use a passive ice protection system (IPS) such as a superhydrophobic coating (SHC) which is able to reduce the droplets permanence on the surface nacelle lip-skin, thereby reducing de facto the accreted ice [11]. Additionally, during the whole flight, the passive SHC could be used in combination with the active PTAI to reduce the needed hot air mass flow, and consequently mitigate some limitations of the active PTAI system, such as the increased fuel consumption, the reduced overall thermal efficiency, and the performance losses.

Several previous studies focused on the simulation study of the effect of PTAI on the lip-skin of the nacelle [3,8,9,12–14], but very little can be found in the literature with regard to the experimental tests in icing wind tunnel (IWT). For example, Papadakis [15] conducted icing tests in the NASA Glenn wind tunnel for a full-sized engine inlet and documented ice shapes on the leading edge under different icing conditions. Tian et al. [16] conducted an experimental campaign to study the dynamic ice accretion on rotating aeroengine spinner and fan blades, with the aim to evaluate the icing-induced performance degradation to the fan rotor. With the perspective to reduce the energy cost of the PTAI system, in [17], the authors carried out an experimental study to quantify the dynamic ice accretion process on aeroengine inlet guide vanes in order to optimize the design paradigms to reduce the requirements of the bleed air. Finally, they also suggested as a novel anti-/de-icing strategy to leverage hydrophobic/icephobic coatings to further reduce the requirements of the bleed air for the inlet guide vanes' anti-/de-icing operation, thereby minimizing the performance penalties to the aeroengines. Studies on the effect of a superhydrophobic surface (SHS) and anti-icing coatings on rotating aeroengine fan blades were reported in [18], where the authors highlighted that both SHS and icephobic coatings have advantages in anti-icing. SHS facilitated the blades' surface with much less ice under both glazed and rimed icing conditions, while icephobic coating prevents large ice-chunk formation in the leading edge as ice chunks easily shed from the leading edge, compared with the SHS blade and blades with a hydrophilic coating.

In this context, the present work reports an experimental test campaign performed in the Italian Aerospace Research Centre (CIRA) IWT with the aim to evaluate the effect of a SHC on the ice accretion occurring on the nacelle lip-skin belonging to the M28 PZL vehicle, possessing dimensions of 50 cm × 50 cm × 20 cm and is made of stainless-steel (the PTAI) and composite (the back side). To the best of our knowledge, no previous work focused on this topic. IWT tests were performed at the takeoff and first climb conditions [9], which represent the worst case for ice accretion due to the switched off PTAI system in these two flight phases, at T = −5 °C and −12 °C, v = 70 and 95 m/s, at an altitude of 3000 m, with a median volumetric diameter (MVD) equal to 20 µm and liquid water content (LWC) equal to 0.3 and 1 g/m^3. Tests were performed before and after the application of a SHC, in order to study the effect of the SHC application on ice accretion. Accreted ice was measured after each test in terms of thickness and impingement length. In a previous work [11], the authors studied the effect of the SHC on the ice accretion occurring on two wing profiles of NACA0015 made of acrylonitrile butadiene styrene and manufactured with a 3D printing machine, having a length of 135 mm and a chord of 100 mm. Broader ranges of IWT parameters were considered in the previous work, i.e., temperatures ranging between −3 °C and −23 °C, speed 50 and 95 m/s, and LWC 0.3 and 0.6 g/m^3.

The present work was developed in the framework of the Clean Sky 2 SAT-AM (More Affordable Small Aircraft Manufacturing) project, whose main goal was to investigate new technologies for a future small aircraft able to fly with low fuel consumption. The reference vehicle for this project was the M28 designed and manufactured by Consortium Partner Polskie Zakłady Lotnicze (PZL), Mielec (PL). It is a commuter category 19 passenger, twin-engine high-wing cantilever monoplane, suited for passenger and/or cargo transportation and certified under EU CS-23 and USA FAR 23 requirements.

2. Materials and Methods

A nanostructured coating developed at CIRA [19,20] was applied with an aerograph using de-humified air at 3 bars, with a layer-by-layer technique. The coating was cured in an autoclave at 80 °C.

Roughness of surfaces before and after the application of the coating was measured by employing a SAMA SA6260 surface roughness meter. Roughness measurements, performed according to the ISO 4288 [21], were reported as Ra, which represents the arithmetic average of the absolute values of the profile height deviations from the mean line.

The optical images were acquired with a microscope USB Dino-Lite AM4815ZTL at 140×.

The contact angle (CA) measurements were performed at 23 °C in compliance with the ASTM D7490-13 [22] standard, with 3 µL of water (H_2O). Contact angles were rapidly acquired within 30 s of depositing the drop to avoid changes in angles.

The thickness of the dry coating was measured according to ISO 2360 [23] using the Defelsko PosiTector 6000 FSN2, manufactured by DeFelsko Corporation, Ogdensburg, NY, USA.

IWT tests were performed in CIRA IWT facility, which is a closed loop circuit, refrigerated wind tunnel with three interchangeable test sections and one open jet configuration, whose main purpose is to perform icing tests. The cloud generation for icing conditions simulation is carried out by the spray bar system (Figure 1), able to generate water droplets with diameters (MVD) and concentrations (LWC) covering nearly the overall envelope prescribed by the Appendix C CS-25 for both continuous and intermittent cloud conditions.

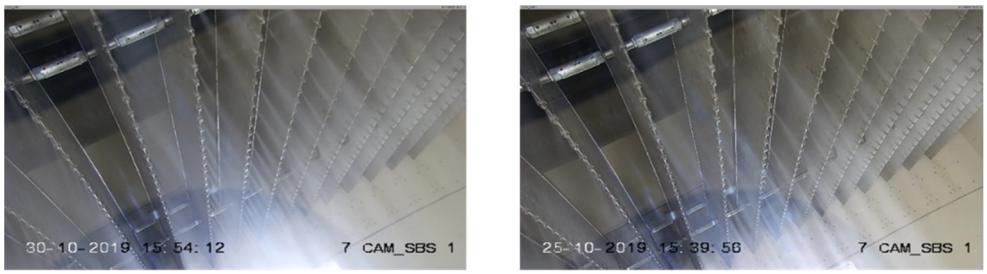

Figure 1. Pattern configurations of spray bar nozzles: 1:2 grid, one half of the spray bar nozzles working (**a**); 1:4 grid, one quarter of spray bar nozzles working (**b**).

Ice accretion measurements were performed after each test. A cold stop at −20 °C guaranteed to freeze the accreted ice on the test article, in order to allow the CIRA team to enter the tunnel, take pictures and measurements of thickness and impingement lengths performed in correspondence to 13 sections drawn before tests on the metallic leading edge (red and blue lines in Figure 2). Measurements of the ice thickness as the difference of measured length section before and after each test taken using a Mitutoyo CD-20DAX digital centesimal caliber, with an accuracy better than 0.02 mm (Figure 3a). For each test condition, the ratios between the mean values of the difference between the ice thicknesses recorded at the measuring stations in coated and uncoated configurations and the mean values of the ice thicknesses measured during the corresponding uncoated tests were evaluated in order to have a quantitative global estimation of the SHC performance on the ice accretion performance in terms of the percentage change of ice accretion thickness. The impingement length of the accreted ice was calculated as the difference between the total length of metallic part and length free from ice (see picture in Figure 3b), measured using the Mitutoyo CD-20DAX digital centesimal caliber. During the measurements, the caliper was aligned with the reference lines drawn before tests on the test article. In Figure 3c, a schematic draw of the accreted compact ice and isolated droplets observed during the IWT test campaign is displayed. Similar to the ice thickness data, for each test condition, the ratios between the mean values of the difference between the impingement length recorded at the measuring stations in coated and uncoated configurations and the mean

values of the impingement length measured during the corresponding uncoated tests were evaluated in order to have a quantitative global estimation of the SHC performance on the impingement length as percentage change of the impingement length. During the measurements (Figure 3a,b) the IWT test section was kept at subzero temperature in order to avoid ice melting.

Figure 2. Sections drawn on the test article before tests.

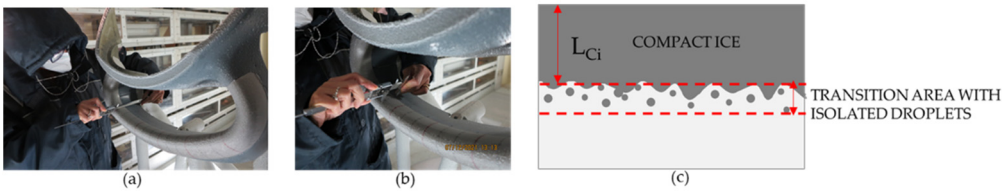

Figure 3. Measurements of thickness measurement (**a**) and of the impingement length (**b**); schematic draw of the accreted compact ice Lci and isolated droplets (**c**).

3. Results

3.1. Superhydrophobic Coating Application

Since paint adheres to rougher surfaces more strongly than to smooth surfaces because of the increased contact area and an interlocking effect, a specific roughness of the test article substrate was required. A previous work [24] established the best roughness at about 3–4 µm achieved through sand blasting. Figure 4a shows the M28 PZL vehicle highlighted in the red circle of the nacelle test article, whereas Figure 4b,c display the nacelle lip-skin before and after the sand blasting useful for achieving the required Ra = 3.2 µm ± 0.2. Figure 4d shows the nacelle lip-skin after the application of the CIRA SHC [19,20], having a thickness of 32 µm ± 6 and a roughness Ra = 1.6 µm ± 0.3.

Figure 4. M28 PZL vehicle (**a**) and nacelle test article before (**b**) and after (**c**) the sand blasting treatment, and after the application of the superhydrophobic coating (**d**).

The test article surface after the sand blasting treatment has a uniform sponge-like morphology (Figure 5a,b) which was preserved after the application of the coating (Figure 5c). This morphology is helpful to guarantee a good adhesion of the coating due to the mechanical interlocking occurring around the interphase substrate-coating. Moreover, the sponge-like morphology preserved after the application of the coating is useful to trap air and contribute to superhydrophobicity [25].

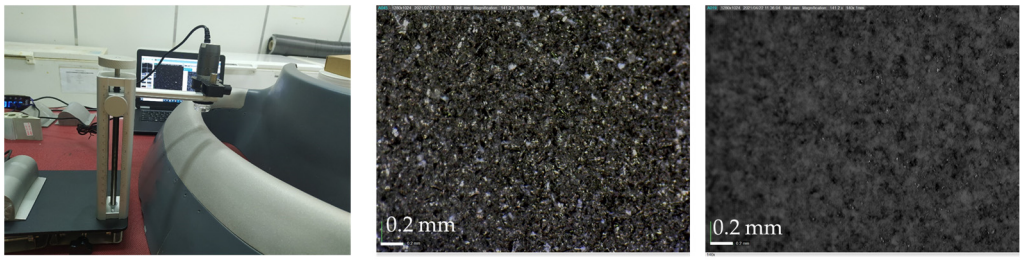

(a) (b) (c)

Figure 5. Set-up for the optical microscopy acquisitions (**a**); microscope images at 140× of the lip-skin nacelle surface before (**b**) and after (**c**) the coating's application.

Figure 6 shows pictures of water droplets on flat samples, representative of the nacelle test article having the same roughness, at 25 °C and −27 °C [24]. Measurements of water contact angles performed at 25 °C give values of 44° and 164° on the uncoated and coated surfaces, respectively (Figure 6a,c). These values seem to be preserved at −27 °C (Figure 6b,d). Wettability measurements have also been performed on the test article before and after the coating application using the set-up in Figure 7a. The test confirmed the measured CA on the uncoated surface; however, due to the low wettability of the applied SHC, it has been impossible to perform the measurements of the wettability on the coated surface since water droplets bounce or roll away from the 3D-coated surface, thereby making the acquisition of the static water contact angle impossible. Therefore, on coated surfaces, the quality of the coating application and its corresponding low wettability were assessed through the slipping and/or the bouncing off of water droplets impacting the coated surface, as shown in Figure 7b,c, where the movement of the water droplet is highlighted by a red arrow.

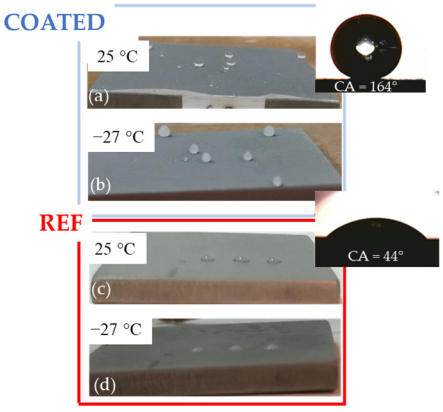

Figure 6. Wettability tests of the coated flat sample representative of the test article performed at 25 °C (**a**) and −27 °C (**b**); wettability of reference performed at 25 °C (**c**) and at −27 °C (**d**) [24].

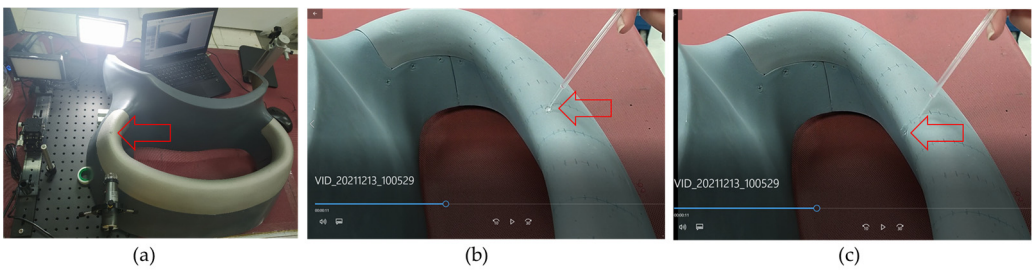

(a) (b) (c)

Figure 7. Wettability test carried out on the test article before (**a**) and after (**b**,**c**) the application of the SHC. The red arrow points at the movement of the water droplet.

3.2. IWT Tests

3.2.1. Installation of Nacelle in the Icing Wind Tunnel

The test article has been installed in the IWT main test section (Figure 8), whose dimensions are: width 2.3 m, height 2.35 m, length 7 m. The test section is equipped with two turntables for model attitude setting; the maximum attainable Mach number is about 0.4 and the minimum static temperature is −32 °C. In this configuration, the model is generally vertically mounted between the wind tunnel floor and ceiling, using as fixing points two interface plates fastened on the two turntables. The interface plates are customized for each test campaign. In this case, only the lower turntable has been used for model installation. The test article was fixed on the interface plate by means of four fixing points, each one made of four M10 bolts.

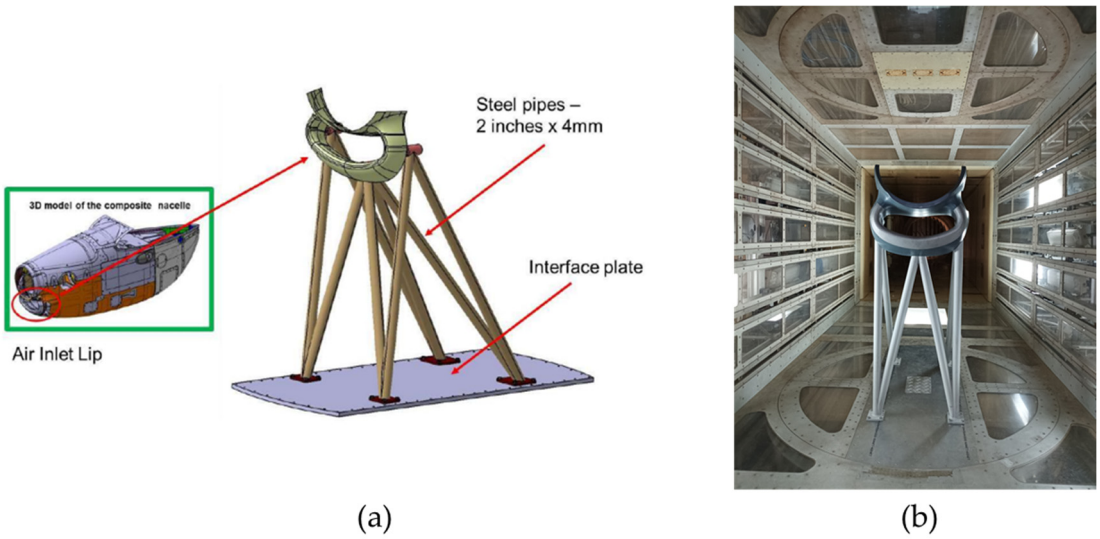

Figure 8. Design of the test article support for the IWT tests (**a**); test article mounted in the IWT facility (**b**).

3.2.2. IWT Test Definition

The M28 PZL is a commuter turboprop airplane, belonging to the CS-23 Normal, Utility, Aerobatic and Commuter Airplanes, that is the 14 CFR, Part 23. According to the 14 CFR Appendix C of Part 25 (Electronic Code of Federal Regulations (eCFR)), the CS-23 class aviation is regulated by the FAR 25 Appendix C, to be used as reference once the aircraft performances are known. The test matrix for the IWT test was defined by taking into account the maximum and the cruise speed of the M28 PZL, which are 355 km/h (98.6 m/s) and 244 km/h (67.8 m/s), respectively, as well as the flight altitude of 3000 m for the cruise altitude, to which corresponds a T = −4.5 °C, according to the standard atmosphere of 1976. For all tests, an MVD of 20 µm and a flight altitude of 3000 m were considered. All other IWT test conditions are detailed in Table 1, which also correspond to the take-off and the first climb conditions of an aircraft CS-25 class aviation [9]. Tests have been performed before on the neat test article (UNCOATED in Table 1), and then, after the application of the SHC, on the coated one (COATED in Table 1). With respect to the baseline, corresponding to the standard temperature of −5 °C, the cruise speed of 70 m/s, an LWC equal to 0.3 g/m^3, and an exposure time of 140 s (test 1–2), the following effects have been analyzed: (a) LWC (equal to 1 g/m^3 in tests 3 and 4), (b) temperature (reduced to −12 °C in tests 5 and 6), (c) exposure time (increased to 420 s in tests 7 and 8), and (d) velocity (increased to the maximum speed equal to 95 m/s in tests 9, 10, and 11). During tests, a humidity ranging from 89% to 93% has been measured. The formation of glaze, rime, and mixed ices was observed [26,27].

Table 1. IWT test conditions.

Test ID	Coating	T [°C]	v [m/s]	Liquid Water Content [g/m^3]	Exposure Time [s]	Flight Path [km]
1	UNCOATED	−5	70	0.3	140	9.8
3		−5	70	1	140	9.8
5		−12	70	0.3	140	9.8
7		−12	70	0.3	420	29.4
9		−5	95	0.3	140	13.3
2	COATED	−5	70	0.3	140	9.8
4		−5	70	1	140	9.8
6		−12	70	0.3	140	9.8
8		−12	70	0.3	420	29.4
10		−5	95	0.3	140	13.3
11		−5	95	0.3	140	13.3

3.2.3. IWT Test Results

In the following, the results related to the IWT tests performed on the coated and uncoated test article are reported.

Test 1–2 T = −5 °C; v = 70 m/s; H = 3000 m; MVD = 20 μm; LWC = 0.3 g/m^3; t = 140 s—Baseline

Tests 1 and 2, performed at −5 °C with a velocity of 70 m/s near the cruise velocity of the M28 PZL vehicle and an LWC of 0.3 g/m^3, represent the base-line tests for the uncoated and coated test article, respectively. Test 1 has been performed on the uncoated surface (Figure 9a–d) and test 2 on the coated one (see results in Figure 9e–h). The pictures taken after the two tests highlighted that in these conditions and for the selected exposure time, i.e., 140 s, the amount of the ice accreted on both uncoated and coated surfaces is poor and concentrated at the impingement area, whereas both inner and outer sides of the nacelle lip-skin were free from ice. Average thickness values of 1.78 mm and 1.16 mm were measured at the uncoated and coated leading edge, respectively. The accreted ice seems similar to dry rime ice [27–29]. Nevertheless, beyond the dense and compact ice, an area with isolated ice droplets appears, as schematically illustrated in Figure 3c, especially for the coated surface. Here, the isolated ice droplets are greater in quantity and size (Figure 9g) than those observed on the uncoated surface. Moreover, they have the same spherical shape as that observed for isolated droplets of ice frozen in static conditions (Figure 6).

Test 3–4: T = −5 °C; v = 70 m/s; H = 3000 m; MVD = 20 μm; LWC = 1 g/m^3; t = 140 s—LWC Effect

In order to study the effect of the LWC, tests 3 and 4 have been performed at an LWC equal to 1 g/m^3. Pictures taken after test 3 of the uncoated test article are shown in Figure 10a–c, whereas pictures of test 4 carried out on the coated test article are displayed in Figure 10d–f. By comparing the pictures in Figure 10 with those in Figure 9 (baseline test), it is highlighted that the effect of increasing the LWC corresponds to an increased amount of accreted ice, which was observed mainly in correspondence to the impingement area and alongside the internal part of the nacelle lip. Here, the ice has accreted as frozen rivulets instead of isolated ice droplets, as observed at the lower LWC. This is due to the larger amount of liquid water as the impacted water mass would only freeze partially, while the remaining water would coalesce into rivulets and run back over the downstream surface. Instead, the ice accreted in a spherical-like shape can be observed only at the impingement line, before the rivulets, on both the uncoated and coated surfaces. They seem to make a separation between the dense ice below them and the rivulets beyond the stagnation line. The formation of this spherical-like ice accumulated at the stagnation line along with the isolated rivulets downstream are typical of glazed ice accretion [27]. The average thickness of ice measured on uncoated and coated surfaces were, respectively, 1.75 mm and 1.74 mm. Measurements of the impingement length of the accreted ice, Lci, reported in Figure 11 reveal that no differences can be observed between the uncoated

and coated surfaces. Rather, the Lci for the uncoated surface seems to be slightly shorter than that measured on the coated surface. Here, the values of Lci measured for the coated surface in Section 8 and uncoated surface in Section 11 are reported as isolated dots and are not included in the trend due to a substantial deviating rate. This deviation could be due to some imperfections in the nacelle surface, highlighted in these tests more than in the others. Finally, by comparing the rivulets' lengths in Figure 10c,f, it is notable that these are much longer and that the rivulets' distribution is denser on the uncoated surface than on the coated one.

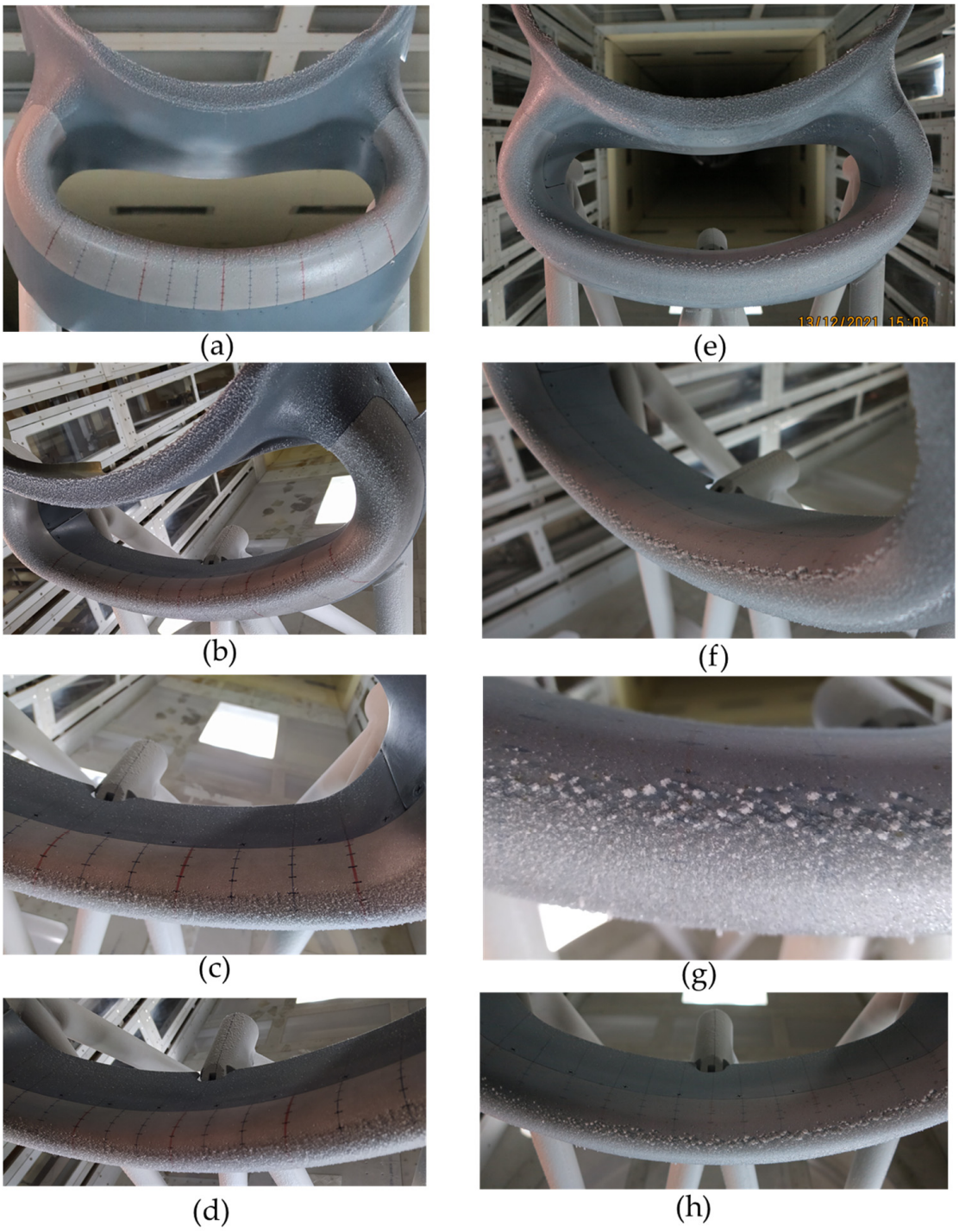

Figure 9. Results of test 1 performed on the uncoated test article (**a**–**d**) and of test 2 carried out on the coated test article (**e**–**h**).

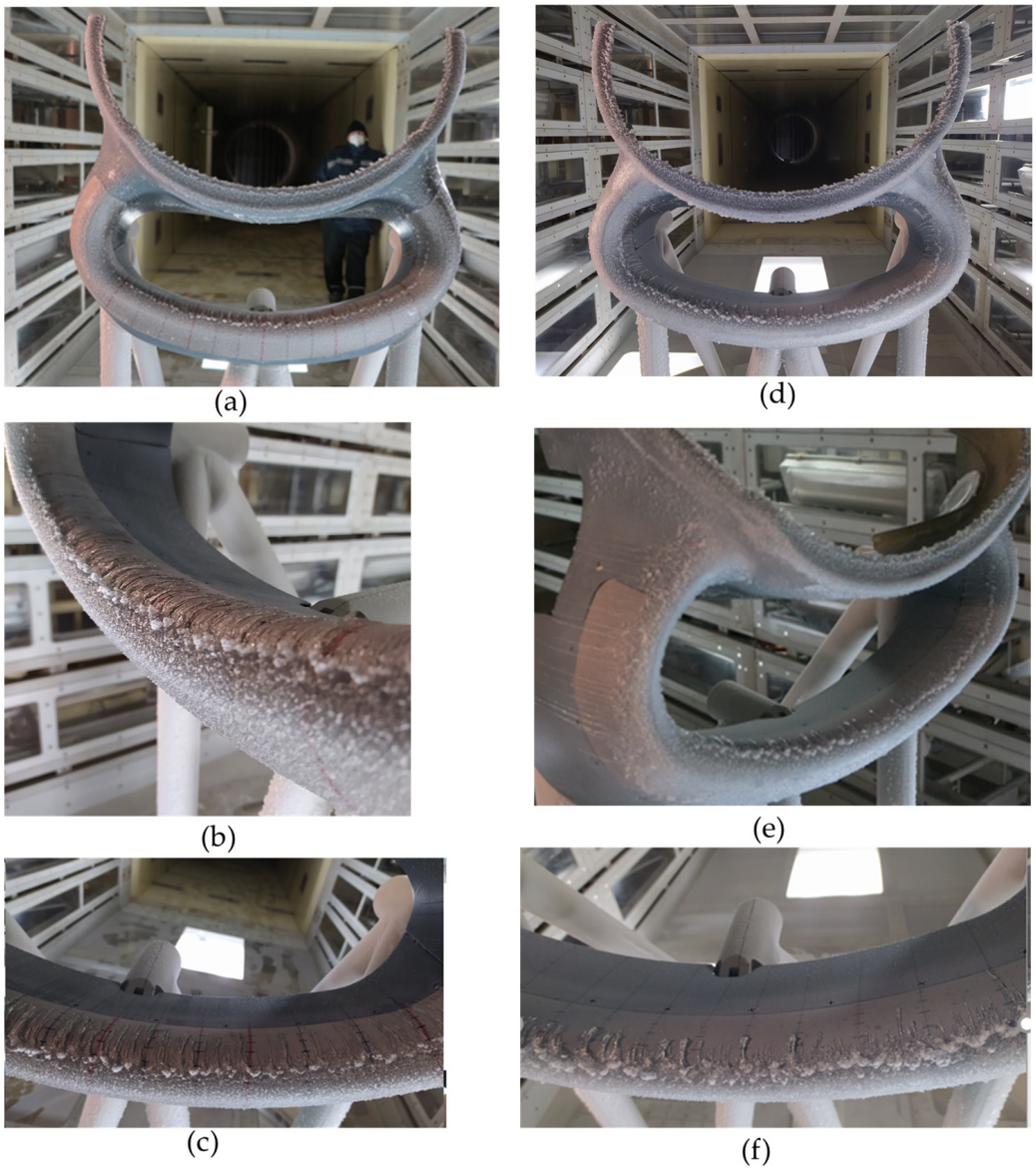

Figure 10. Results of test 3 (**a**–**c**) on uncoated surface of test article and test 4 (**d**–**f**) on coated surface of test article.

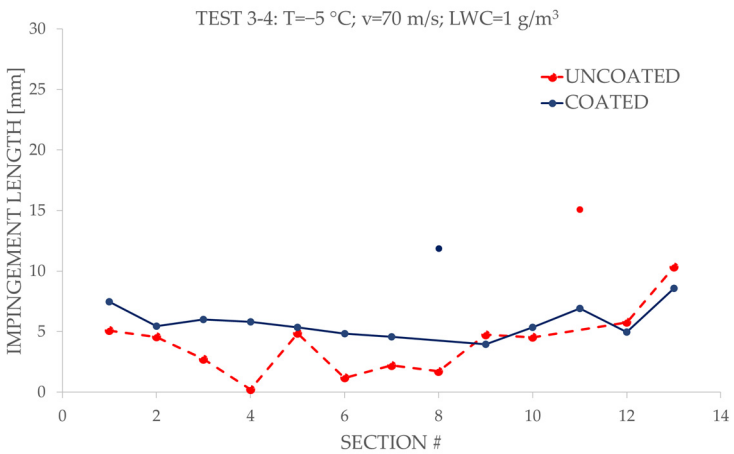

Figure 11. Impingement length measured after tests 3 and 4.

Test 5–6: T = −12 °C; v = 70 m/s; H = 3000 m; MVD = 20 μm; LWC = 0.3 g/m^3; t = 140 s—T Effect (Baseline for Tests 7 and 8)

The effect of the decreased temperature was assessed with tests performed at −12 °C. Pictures of tests performed on uncoated and coated surfaces are displayed in Figure 12a–j, respectively. As for baseline tests 1 and 2, sparse ice droplets having spherical shapes appear on both coated and uncoated surfaces, displaying a typical dry rime ice accretion [27]. However, the coated surface has more isolated ice droplets, which result in a less dense transition area, and the ice droplets have larger dimensions than those accreted on the uncoated surface. Average thicknesses of accreted ice on uncoated and coated surfaces were 1.51 mm and 0.77 mm, respectively. No significant difference can be observed in the impingement lengths (see Figure 13).

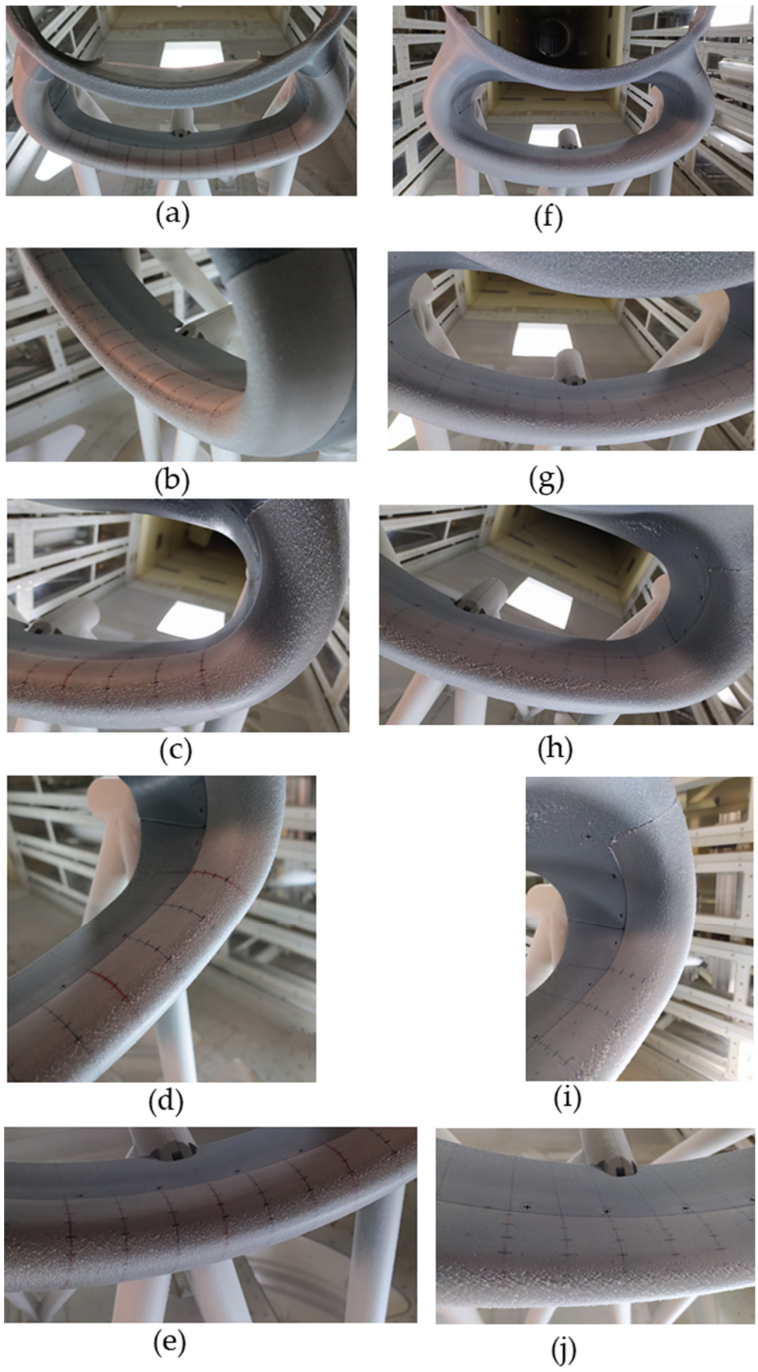

Figure 12. Results of test 5 (**a**–**e**), on uncoated test article and test 6 (**f**–**j**) on coated test article.

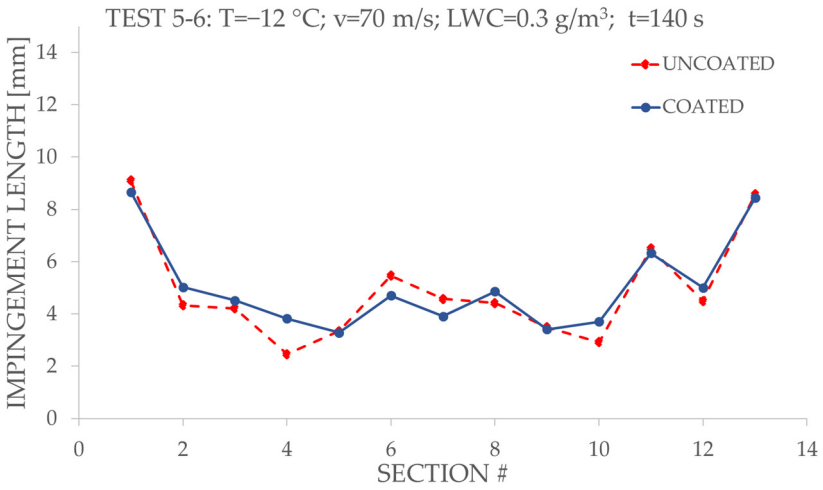

Figure 13. Impingement length measured after test 5 and test 6.

Test 7–8: T = −12 °C; v = 70 m/s; H = 3000 m; MVD = 20 μm; LWC = 0.3 g/m^3; t = 420 s—Exposure Time and Temperature Effect

Starting from tests 5 and 6 performed at −12 °C, the exposure time was increased to 420 s. Pictures of tests 7 and 8, performed on uncoated and coated surfaces, were shown in Figure 14a–j, respectively. By comparing pictures in Figure 12 at a shorter exposure time with those of Figure 14, it can be observed that the ice accumulated on both uncoated and coated surfaces increases as the exposure time increases, as expected. The accreted ice assumes two different shapes: it is milky with crystalline structures on the upstream area, typical of rime ice, whereas it appears to be less dense with columnar structures at the stagnation line, typical of glaze ice [27,29]. Quite no differences can be observed in the shape and appearance of the ice grown on coated and uncoated surfaces. However, it was found that the impingement length of ice accreted on the coated surface is on average 3 mm shorter than that measured on the uncoated surface (Figure 15). Finally, measured thickness was 3.46 mm and 2.97 mm for uncoated and coated surfaces, respectively.

Test 12–13–14: T = −5 °C; v = 95 m/s; H = 3000 m; MVD = 20 μm; LWC = 0.3 g/m^3; t = 140 s—V Effect

Velocity was increased to 95 m/s in tests 9 and 10; pictures of results are displayed in Figure 16a–d for uncoated and Figure 16e–h for coated test article. A test of repeatability was performed on the coated surface (test 11), and results are shown in Figure 17. Compared with the baseline tests (Figure 9), it was found that as the incoming flow velocity increased, the water droplets on the uncoated surface would move more rapidly downstream and then freeze as thin and narrow runback rivulets due to the increased aerodynamic stress acting on the rivulet flows, as observed also by Gao et al. [27]. A striking contrast is the dynamic of icing on the coated surface. Here, the formation of rivulets stopped at the beginning phase (see Figure 16f,g and Figure 17g,h), and the area downstream was free of ice. As a consequence, the impingement length of compact ice Lci was reduced on an average of 4 mm with respect to the uncoated surface, as shown in Figure 18. Far from the impingement line, on the right and left sides of the test article and in the area below the impingement line, the formation of isolated, spherical, and large frozen water droplets were observed only on the coated surface (Figures 16h and 17b,f). A repeatability test performed on the coated test article confirms both the accreted ice shape (Figure 17) and the measured length of the compact ice (Figure 18). Measurements of thickness provided average values of 1.10 mm for the uncoated test, and 0.90 mm and 0.81 mm for the two coated tests.

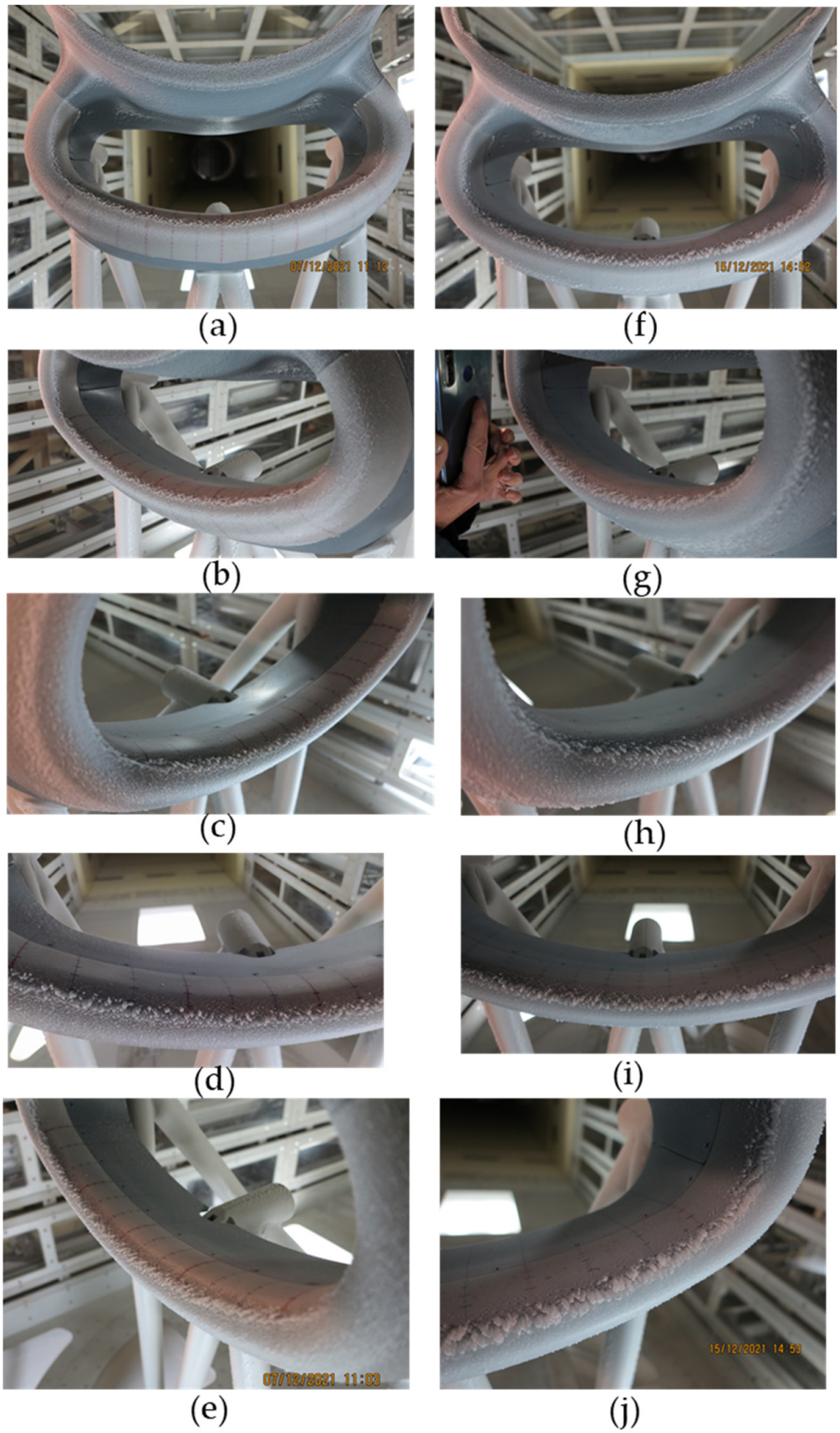

Figure 14. Results of test 7 (**a**–**e**) on uncoated test article and test 8 (**f**–**j**) on coated test article.

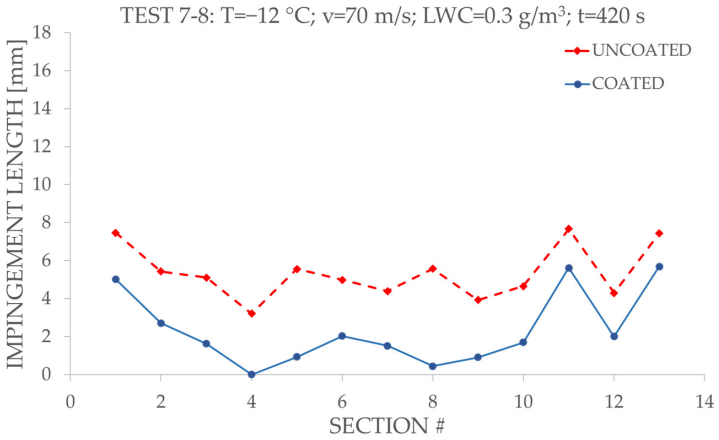

Figure 15. Impingement length measured after tests 7 and 8.

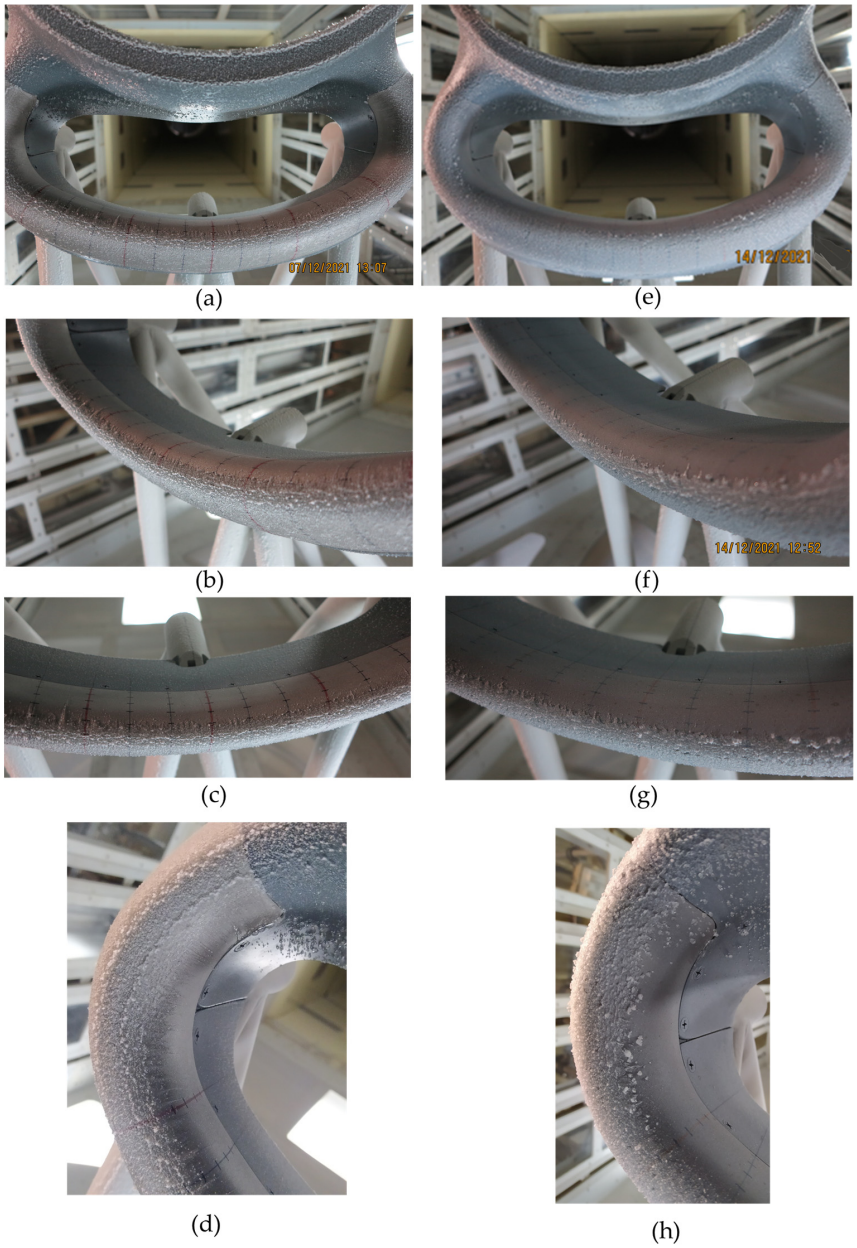

Figure 16. Results of test 9 (**a**–**d**) on uncoated test article and test 10 (**e**–**h**) on coated test article.

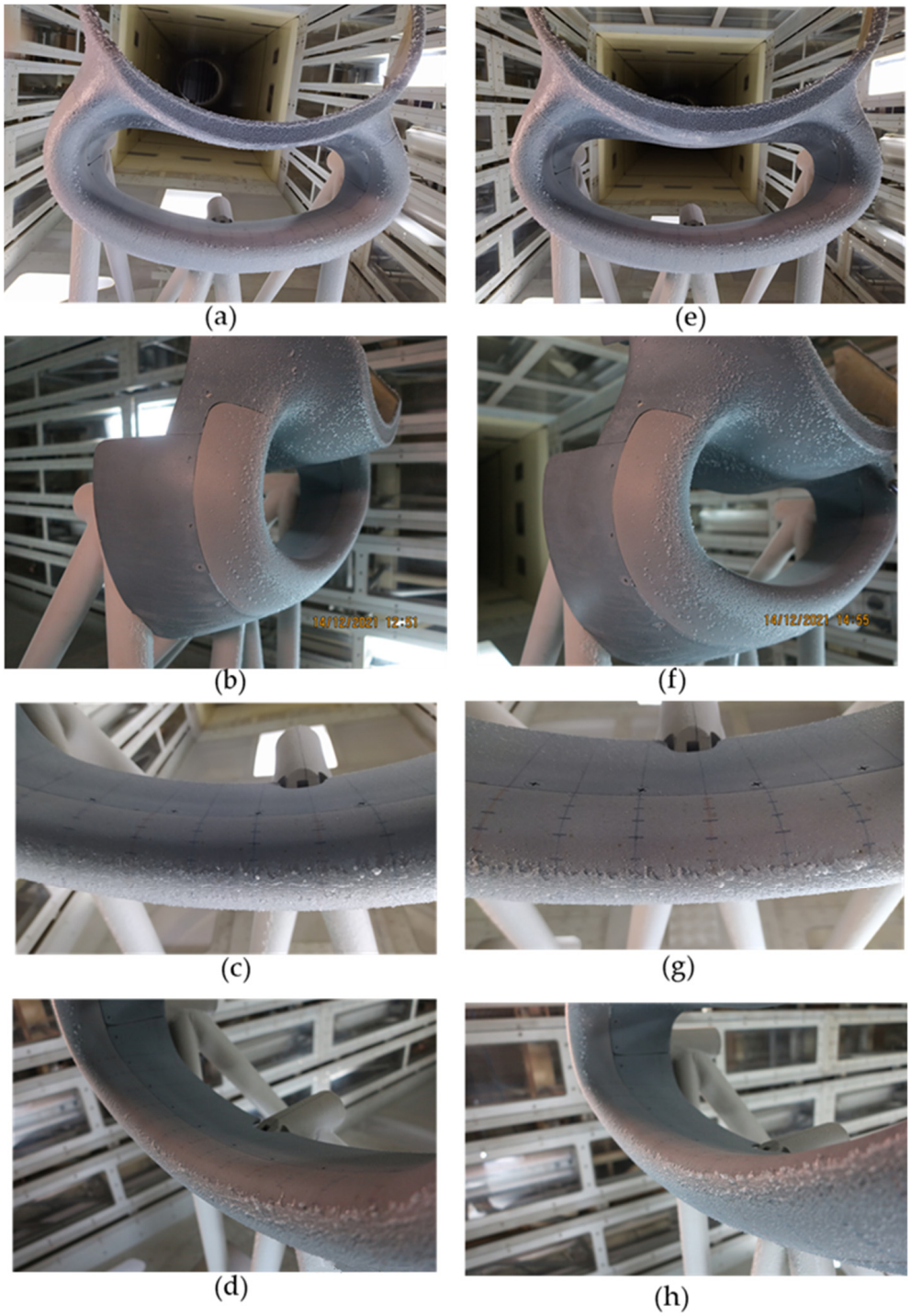

Figure 17. Repeatability test results on coated test article: test 10 (**a**–**d**) and test 11 (**e**–**h**).

3.3. Wettability after Icing/De-icing Cycles

Pictures of the test article after the IWT tests shown in Figure 19 highlight that the distribution of the SHC seems to be ununiform as after recent application, but the milky color of the coating resembles a leopard-spot distribution. However, the low wettability of all the test article surfaces was preserved since water droplets impacting it rapidly bounce and slide off (Figure 20).

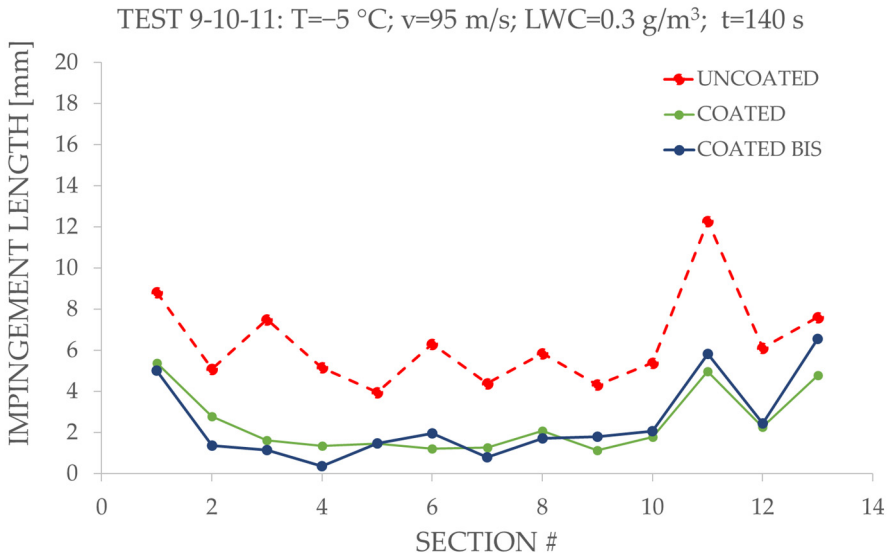

Figure 18. Impingement length measured after tests 9, 10, and 11.

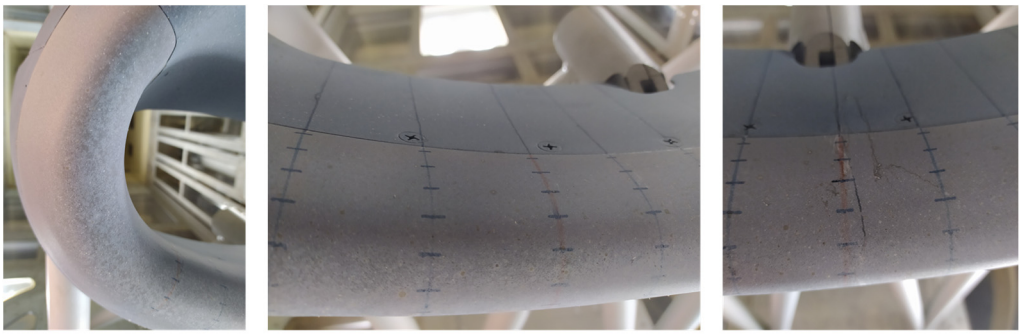

Figure 19. Images of the coated surface of the test article after IWT test campaign; left side of the test article (**a**); middle side of test article (**b**,**c**).

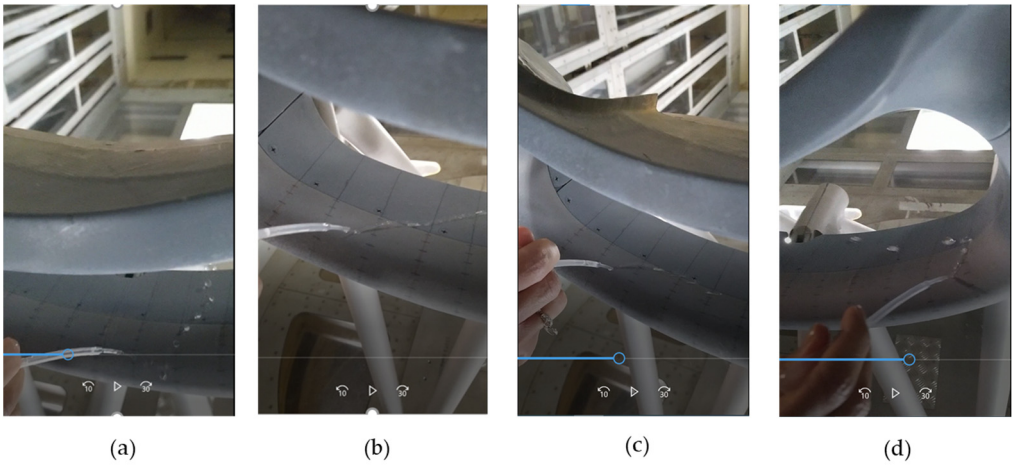

Figure 20. Wettability test performed on the test article after the IWT test campaign (**a**–**d**).

4. Discussion

Pictures of ice accreted on the uncoated and coated surfaces acquired after tests can be meaningful and useful to understand the different icing dynamics. A summary of the IWT test campaign results is shown in Figure 21.

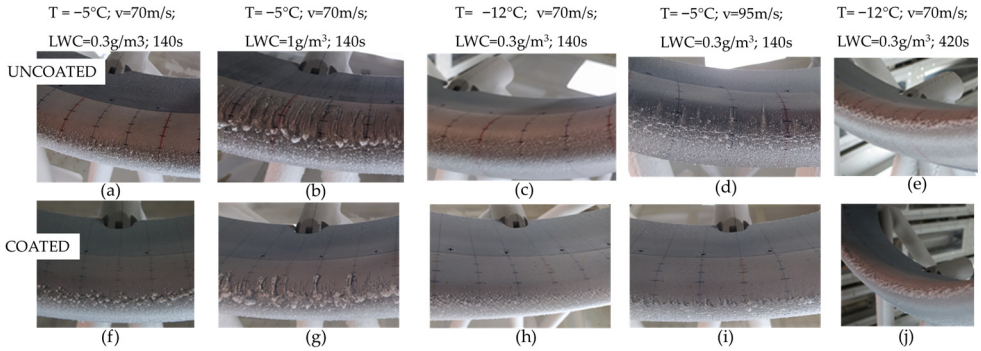

Figure 21. Summary of the IWT test campaign results found on uncoated (**a**–**e**) and coated (**f**–**j**) surfaces of the test article.

It appears that one difference raised during the IWT tests between coated and uncoated surfaces is the presence of isolated ice droplets observed especially on coated surfaces and in tests 1–2 (Figures 9, 12 and 21a,f,c,h). The presence of isolated frozen water droplets can be ascribed to the low wettability and consequently the low rolling angles [30] of coated surfaces, so the water droplets impacting the coated surface quickly bounce on it and/or slide off. Thus, depending on the test conditions, they take a longer path before freezing or not freeze at all. From a microscopic perspective, this evidence could be explained with the classical nucleation theory [31,32], according to which the larger the contact angle is, the larger the free energy barrier ΔG for the formation of ice nucleus and the smaller the nucleation rate J, so the nucleation becomes more difficult and slower. The small contact area of the applied SHC and the dynamic behavior of water droplets reduce the probability of nucleation, thus reducing the probability of ice on the surface. As a matter of fact, the isolated ice droplets observed on the coated surface are located at a bigger distance from the impingement area with respect to the uncoated one, thereby increasing de facto the transition area (see for instance Figure 9 and scheme in Figure 3c). Another remarkable finding is that the isolated ice droplets accreted on the coated surface have a spherical shape and larger dimensions than those frozen on the uncoated surface. The shape of the isolated ice droplets on the coated surface can be ascribed to the low wettability of SHC at low temperature (Figure 6), so the surface also retains the Cassie–Baxter state at low temperature, whereas the larger dimensions could be explained by imagining that the fewer water droplets frozen on the coated surface become ice nucleation points, causing the other incoming droplets to freeze on them, thus increasing their dimensions. The high-humidity environment of test conditions [33] and some surface imperfections could be the reason why there is a transition from the Cassie–Baxter to the Wenzel state with penetration and condensation into the surface cavities [33]. Therefore, these microdroplets nucleate and grow, becoming anchoring points for further incoming water droplets. The authors observed the same behavior in other previous IWT tests [11] performed on two-wing profiles NACA0015 tested at temperatures ranging between −3 °C and −23 °C, speed 50 and 95 m/s, and LWC 0.3 and 0.6 g/m^3. Here, the isolated and spherical water droplets were observed in all tests performed at temperatures higher than −12 °C.

At low temperature, sparse ice droplets appear on both coated and uncoated surfaces, displaying a typical dry rime ice accretion [27]. Once again, the presence of isolated ice droplets which reduce the density of the transition area can be observed especially on the coated surface, but compared to the baseline tests at −5 °C, at −12 °C, this phenomenon is largely reduced and the larger isolated ice droplets are relatively absent (Figure 21a,f,c,h). This is most likely because the lower temperature allows the water droplets to freeze immediately upon impact with the surface, so their sliding off is hugely reduced. This evidence agrees with studies from Xu et al. [34], according to which the frosting time reduces as the temperature reduces.

Increase in exposure time at low temperature has the effect to increase the accumulated ice, as expected, and no differences can be observed in the shape and appearance of ice accreted on coated and uncoated surfaces (Figure 21e,j).

The major advantage in applying a SHC can be highlighted at a higher LWC and higher velocity, where the nucleation is more difficult and slower for SHC with respect to the uncoated surface [31,32]. At a higher LWC, the isolated ice droplets disappear and, in their place, several ice rivulets appear alongside the internal part of the nacelle lip (Figure 21b,g). The presence of rivulets on both uncoated and coated surfaces is due to the increased amount of impacted liquid water, which would only freeze partially, while the remaining water would coalesce into rivulets and run back over the downstream surface [27]. Figure 21b,g highlight a prominent difference in the length of rivulets frozen on coated and uncoated surfaces ascribed once again to the low wettability of the applied SHC, which allows the liquid water to slide off before freezing, thereby reducing the length of the frozen rivulets. At the impingement line, the impacting water quickly freezes, accreting as spherical-like ice regardless of the wettability of the surface. This is because at the impingement line, no helpful forces are present to take advantage from the low wettability of the SHC and allow water to slide off.

On the other hand, at a higher velocity, the high-speed water droplets colliding with the test article surface do not get enough time to freeze. Incoming airflow pushes these droplets further away from the stagnation line which leads, on the uncoated surface, to the accumulation of these droplets along upper and lower sides of the stagnation line as thin and narrow runback rivulets. In contrast to the uncoated surface, the high-speed water droplets for the coated surface slip away rapidly without freezing at all downstream the stagnation line (Figure 21d,i), and so reducing de facto the length of the accreted compact ice Lci, leaving the area upper the stagnation line free of ice.

A direct comparison between the present and the previous [11] IWT test campaign can be made only between the test performed at higher velocity, namely at −5 °C, v = 95 m/s, LWC = 0.3 g/m^3, and exposure time = 140 s, and the previous one carried out at −6 °C, v = 95 m/s, LWC = 0.3 g/m^3, and exposure time = 137 s (test 3 in [11]). Ascribed to the different geometrical configuration of the two test articles, many differences can be observed for the ice accumulated on both the uncoated and coated surfaces of the test article. In fact, instead of thin and narrow runback rivulets, in the previous work, a typical dry rime ice accretion can be observed on the uncoated surface, with ice droplets which become less dense and isolated on the coated one. On the contrary, in the present work, the isolated frozen water droplets can be seen only at the inner left and right sides of the test article (Figure 16h).

Figure 22 displays the percentage change of the ice thickness and the impingement length calculated for each test conditions as ratios between the mean values of the differences between measurements taken on coated and uncoated configurations and the mean values of those acquired on the uncoated configuration, showing the effect of the main investigated parameters (LWC, T, exposure time and airspeed).

Results highlight a reduction in the ice thickness accreted on the coated surfaces with respect to the uncoated one across the entire spectrum of test conditions investigated. The maximum ice thickness reduction, i.e., −49%, which was recorded during the tests at −12 °C, matched to an increase in the impingement length of 0.5%. Significant ice thickness and ice impingement length reductions have been recorded in the tests aimed to evaluate the airspeed and the exposure time. In particular, the application of the SHC allows the ice thickness to be reduced to values of −27% and −14%, at 95 m/s and at 420 s of exposure time, respectively. The impingement length reductions were −9.6% and −7.6%, respectively. The repeatability tests performed at higher airspeed show a good agreement between them, corroborating the overall quality of the carried-out measurements. Finally, the test aimed to assess the LWC effect presents a moderate reduction in the ice thickness, i.e., −8%, matched to an increase in the impingement length, i.e., 3.7%. Nevertheless, the

relevant finding at a higher LWC is the reduced length and number of the ice rivulets observed for the coated configuration.

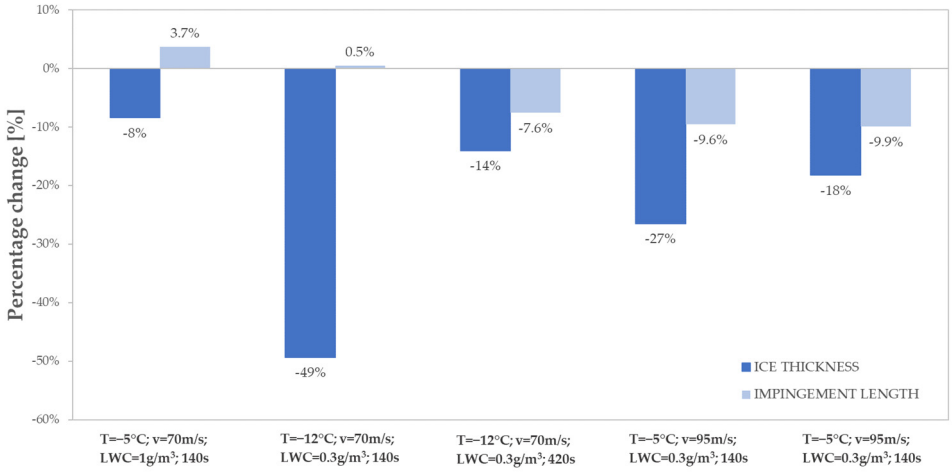

Figure 22. Percentage change of ice thickness and impingement length measured at investigated test conditions.

Ultimately, the lesson learned from the two IWT test campaigns is that the low wettability of the SHC reduces the permanence time of water droplets on surfaces and the probability of icing on the coated surfaces with respect to the uncoated ones, but the thickness and the impingement length of the accreted ice largely depend on the geometrical configuration of the test article. As a consequence, it was found that the ice thickness variations observed in the previous work [11] for tests carried out at temperatures ranging between −3 °C and −12 °C varied from −3% to −34% and from +5% to −5% for A1 and A2 coated configurations, respectively, whereas in the present work, the ice thickness reduction is more pronounced, ranging between −8% and −49%. On the other hand, the impingement length reduction with respect to the uncoated surfaces in the previous work [11] ranged between −35% and −100% for A1, and −12% and −76% for A2, which becomes less pronounced in the present work, ranging between +3.7% and −10%.

5. Conclusions

This work provides and discusses results of an icing wind tunnel (IWT) experimental campaign performed on a nacelle lip-skin belonging to the M28 Polskie Zakłady Lotnicze (PZL) vehicle. The test campaign reproduced the typical flight conditions of the M28 vehicle, which also correspond to the take-off and first climb conditions of an aircraft CS-25 class aviation. Tests were repeated after the application on the nacelle of a superhydrophobic coating (SHC), in order to study the effect of a low wettability surface on the ice accretion in real flight conditions. SHC performance seems to be encouraging across the entire spectrum of test conditions investigated. The maximum ice thickness reduction was recorded during the tests at lower temperature. Significant ice thickness and ice impingement reduction were also recorded in the tests aimed to evaluate the airspeed and the exposure time. The repeatability tests performed at higher airspeed show a good agreement between them, corroborating the overall quality of the carried-out measurements. Finally, the tests aimed to assess the LWC effect presents a moderate reduction in the ice thickness, matched to an increase in the impingement length but with a reduced length and number of the frozen rivulets.

Future works should focus to further explore the working envelope of SHC, investigating additional test conditions, particularly in terms of LWC and MVD. Future developments should also include the improvement of the measurement technique. The adopted method provided data of appropriate quality for the scope of the intended analysis. Nevertheless, for a deeper understanding of SHC behavior, it is necessary to adopt a measurement tech-

nology able to provide a more substantial amount of quantitative data. The employment of a 3D laser scanner is actually deemed as one of the best possible options. This research is especially relevant for Northern Europe, which is characterized by high humidity.

6. Patents

Data reported in this manuscript refer to coatings whose formulation is protected by the patent submission: F. Piscitelli, Italian Patent Application N. IT102021000032444, "Rivestimento superidrofobico e ghiacciofobico di un substrato, metodo per il suo ottenimento e substrato così rivestito", 23 December 2021, and F. Piscitelli, Substrate superhydrophobic and icephobic coating, method for obtaining it and substrate thus coated, International Patent Application N° PCT/IB2022/062672 22 December 2022.

Author Contributions: Conceptualization, F.P.; methodology, F.P., S.P. and F.D.N.; investigation, F.P. and S.P.; manufacturing F.P. and F.D.N.; data curation, F.P., S.P. and F.D.N.; writing—original draft preparation, F.P.; writing—review and editing, F.P. All authors have read and agreed to the published version of the manuscript.

Funding: This research was funded by Clean Sky JTICS2- 2015-CPW02-AIR-02-07 as SAT-AM (More Affordable Small Aircraft Manufacturing) project.

Institutional Review Board Statement: Not applicable.

Informed Consent Statement: Not applicable.

Data Availability Statement: Not applicable.

Acknowledgments: The author would like to thank Antonio Chiariello for his management support, Antonio Ragni and Antonio Auletta for the interesting discussions and the IWT team for their valuable support during tests.

Conflicts of Interest: The authors declare no conflict of interest.

References

1. Papadakis, M.; Breer, M.; Craig, N.; Liu, X. Experimental Water Droplet Impingement Data on Airfoils, Simulated Ice Shapes, an Engine Inlet and a Finite Wing. *NASA Contract. Rep.* **1994**, 4636–4816.
2. Bidwell, C.S.; Mohler, S.R. Collection efficiency and ice accretion calculation for a sphere, a Swept MS (1)-317 Wing, a Swept NACA-0012 Wing Tip, an Axisymmetric Inlet and Boeing 737-300 Inlet. In Proceedings of the 33rd Aerospace Science Meeting and Exhibit sponsored by the AIAA, Reno, NV, USA, 9–12 January 1995; pp. 95–0755.
3. Ismail, M.A.; Abdullah, M.Z. Applying Computational Fluid Dynamic to Predict the Thermal Performance of the Nacelle Anti-Icing System in Real Flight Scenarios. *Indian. J. Sci. Technol.* **2015**, *8*, 30. [CrossRef]
4. Hua, J.; Liu, H.T. Fluid Flow and thermodynamic analysis of a wing anti-icing system. *Can. Aeronaut. Space J.* **2005**, *51*, 35–40. [CrossRef]
5. Brown, J.M.; Raghunathan, S.; Watterson, J.K. Heat transfer correlation for anti-icing system. *J. Aircr.* **2002**, *39*, 65–70. [CrossRef]
6. Raghunathan, S.; Benard, E.; Watterson, J.K.; Cooper, R.K.; Curran, R.; Price, M.; Yao, H.; Devine, R.; Crawford, B.; Riordan, D.; et al. Key aerodynamic technologies for aircraft engine nacelles. *Aeronaut. J.* **2006**, *110*, 265–288. [CrossRef]
7. Brown, J.M. Investigation of Heat Transfer between a Staggered Array of Hot Air Jets and a Jet Engine Nacelle Lip Skin Surface. Ph.D. Thesis, Queens University Belfast, Belfast, UK, 1999.
8. Syed, M.H.Y.; Ismail, M.A.; Azam, Q.; Rajendran, P.; Mazlan, N.M. Simulation Study of the Effect of Anti-Icing on the Nacelle Lip-skin Material IOP Conf. Ser. *Mater. Sci. Eng.* **2018**, *370*, 012011.
9. Yang, Q.; Guo, X.; Dong, W.; Wang, A. Ice accretion and aerodynamic effects on a turbofan engine nacelle under takeoff conditions. *Aerosp. Sci. Technol.* **2022**, *126*, 107571–107584. [CrossRef]
10. FA Regulation. *Airworthiness Standard: Transport Category Airplanes Part 25 Appendix C*; Federal Aviation Administration, Atlantic City International Airport: Atlantic City, NJ, USA, 1982.
11. Piscitelli, F. Characterization in Relevant Icing Conditions of Two Superhydrophobic Coatings. *Appl. Sci.* **2022**, *12*, 3705. [CrossRef]
12. Khai, L.C.; Ismail, M.A.; Azam, Q.; Mazlan, N.M. Experimental study on aerodynamic performance of nacelle lip-skin bias flow. *J. Mech. Sci. Technol.* **2020**, *34*, 1613–1621. [CrossRef]
13. Hamid, H.A.; Yong, W.K.; Yusoff, H.; Ismail, M.A. CFD Impingement Flow Study on Temperature Profile of Concave Plate. *J. Adv. Res. Fluid. Mech.* **2022**, *95*, 1–16.
14. Özgen, S.; Canıbek, M. In-flight ice formation simulation on finite wings and air intakes. *Aeronaut. J.* **2012**, *116*, 337–362. [CrossRef]
15. Papadakis, M.; Yeong, H.W.; Wong, S.C.; Wong, S.H. Comparison of experimental and computational ice shapes for an engine inlet. In Proceedings of the AIAA Atmospheric and Space Environments Conference, Toronto, ON, Canada, 2–5 August 2010.

16. Tian, L.; Li, L.; Hu, H.; Hu, H. Experimental Study of Dynamic Ice Accretion Process over Rotating Aeroengine Fan Blades. *J. Thermophys. Heat Trans.* **2022**, *37*, 353–364. [CrossRef]
17. Li, L.; Liu, Y.; Tian, L.; Hu, H.; Hu, H.; Liu, X.; Hogate, I.; Kohli, A. An experimental study on a hot-air-based anti-/de-icing system for aeroengine inlet guide vanes. *Appl. Therm. Eng.* **2020**, *167*, 114778–114790. [CrossRef]
18. Tian, L.; Liu, Y.; Li, L.; Hu, H. *An Experimental Study to Evaluate Hydro-/Ice-Phobic Coatings for Icing Mitigation over Rotating Aero-engine Fan Blades*; SAE Technical Paper; SAE International: Warrendale, PA, USA, 2019.
19. Piscitelli, F. Rivestimento Superidrofobico e Ghiacciofobico di un Substrato, Metodo per il suo Ottenimento e Substrato Così Rivestito. Italian Patent Application N. IT102021000032444, 23 December 2021.
20. Piscitelli, F. Substrate Superhydrophobic and Icephobic Coating, Method for Obtaining it and Substrate thus Coated. International Patent Application N° PCT/IB2022/062672, 22 December 2022.
21. *ISO 4288*; Geometrical Product Specifications (GPS)–Surface Texture: Profile Method–Rules and Procedures for the Assessment of Surface Texture. International Organization for Standardization: Geneva, Switzerland, 1996.
22. *D7490-13*; Standard Test Method for Measurement of the Surface Tension of Solid Coatings, Substrates and Pigments using Contact Angle Measurements. American Society for Testing and Materials: West Conshohocken, PA, USA, 2013.
23. *ISO 2360:2017*; Non-Conductive Coatings on Non-Magnetic Electrically Conductive Base Metals—Measurement of Coating Thickness—Amplitude-Sensitive Eddy-Current Method. International Organization for Standardization: Geneva, Switzerland, 2003.
24. Piscitelli, F.; Chiariello, A.; Dabkowski, D.; Corraro, G.; Marra, F.; Di Palma, L. Superhydrophobic Coatings as Anti-Icing Systems for Small Aircraft. *Aerospace* **2020**, *7*, 2. [CrossRef]
25. Piscitelli, F.; Tescione, F.; Mazzola, L.; Bruno, G.; Lavorgna, M. On a simplified method to produce hydrophobic coatings for aeronautical applications. *Appl. Surf. Sci.* **2019**, *472*, 71–81. [CrossRef]
26. Przybyszewski, B.; Kozera, R.; Krawczyk, Z.D.; Boczkowska, A.; Dolatabadi, A.; Amer, A.; Sztorch, B.; Przekop, R.E. A Wind Tunnel Experimental Study of Icing on NACA0012 Aircraft Airfoil with Silicon Compounds Modified Polyurethane Coatings. *Materials* **2021**, *14*, 5687. [CrossRef]
27. Gao, L.; Liu, Y.; Hu, H. An experimental investigation of dynamic ice accretion process on a wind turbine airfoil model considering various icing conditions. *Int. J. Heat. Mass. Transf.* **2019**, *133*, 930–939. [CrossRef]
28. Jin, J.Y.; Virk, M.S. Study of ice accretion and icing effects on aerodynamic characteristics of DU96 wind turbine blade profile. *Cold Reg. Sci. Technol.* **2019**, *160*, 119–127. [CrossRef]
29. Özgen, S.; Canıbek, M. Ice accretion simulation on multi-element airfoils using extended messinger model. *Heat. Mass. Transf.* **2009**, *45*, 305–322. [CrossRef]
30. Li, W.; Zhan, Y.; Yu, S. Applications of superhydrophobic coatings in anti-icing: Theory, mechanisms, impact factors, challenges and perspectives. *Prog. Org. Coat.* **2021**, *152*, 106117–106135. [CrossRef]
31. Varanasi, K.K.; Hsu, M.; Bhate, N.; Yang, W.; Deng, T. Spatial control in the heterogeneous nucleation of water. *Appl. Phys. Lett.* **2009**, *95*, 094101. [CrossRef]
32. Varanasi, K.K.; Deng, T.; Smith, J.D.; Hsu, M.; Bhate, N. Frost formation and ice adhesion on superhydrophobic surfaces. *Appl. Phys. Lett.* **2010**, *97*, 234102. [CrossRef]
33. Yin, L.; Zhu, L.; Wang, Q.; Ding, J.; Chen, Q. Superhydrophobicity of natural and artificial surfaces under controlled condensation conditions. *ACS Appl. Mater. Interfaces* **2011**, *3*, 1254–1260. [CrossRef] [PubMed]
34. Xu, W.J.; Song, J.L.; Sun, J.; Dou, Q.L. Characteristics of ice and frost formation on superhydrophobic surfaces on aluminum substrates. *J. Refrig.* **2011**, *32*, 9–13.